

Article

Nearly 90% Circularly-Polarized Emission in Monolayer WS₂ Single Crystals by Chemical Vapor Deposition

Wei-Hsiang Lin, Wei-Shiuan Tseng, Cora M. Went, Marcus L Teague, George R. Rossman, Harry A Atwater, and Nai-Chang Yeh

ACS Nano, **Just Accepted Manuscript** • DOI: 10.1021/acsnano.9b05550 • Publication Date (Web): 23 Aug 2019

Downloaded from pubs.acs.org on August 23, 2019

Just Accepted

“Just Accepted” manuscripts have been peer-reviewed and accepted for publication. They are posted online prior to technical editing, formatting for publication and author proofing. The American Chemical Society provides “Just Accepted” as a service to the research community to expedite the dissemination of scientific material as soon as possible after acceptance. “Just Accepted” manuscripts appear in full in PDF format accompanied by an HTML abstract. “Just Accepted” manuscripts have been fully peer reviewed, but should not be considered the official version of record. They are citable by the Digital Object Identifier (DOI®). “Just Accepted” is an optional service offered to authors. Therefore, the “Just Accepted” Web site may not include all articles that will be published in the journal. After a manuscript is technically edited and formatted, it will be removed from the “Just Accepted” Web site and published as an ASAP article. Note that technical editing may introduce minor changes to the manuscript text and/or graphics which could affect content, and all legal disclaimers and ethical guidelines that apply to the journal pertain. ACS cannot be held responsible for errors or consequences arising from the use of information contained in these “Just Accepted” manuscripts.

1
2
3
4
5
6
7 Nearly 90% Circularly-Polarized Emission in Monolayer WS₂
8
9
10 Single Crystals by Chemical Vapor Deposition
11
12
13
14

15 Wei-Hsiang Lin,[†] Wei-Shiuan Tseng,[‡] Cora M. Went,[‡] Marcus L. Teague,[‡] George. R.

16
17
18 Rossman,[§] Harry A. Atwater^{†,||} and Nai-Chang Yeh^{*‡,||}
19
20
21
22

23 *Corresponding author, ncyeh@caltech.edu
24
25
26

27 †Department of Applied Physics, California Institute of Technology, Pasadena, CA
28
29

30 91125, USA
31
32
33
34

35 ‡Department of Physics, California Institute of Technology, Pasadena, CA 91125, USA
36
37
38
39

40 §Division of Geological and Planetary Sciences, California Institute of Technology,
41
42

43 Pasadena, A 91125, USA
44
45
46
47

48 ||Kavli Nanoscience Institute, California Institute of Technology, Pasadena, CA 91125,
49
50

51 USA
52
53
54
55
56
57
58
59
60

1
2
3
4
5
6
7
8
9
10
11
12
13
14
15
16
17
18
19
20
21
22
23
24
25
26
27
28
29
30
31
32
33
34
35
36
37
38
39
40
41
42
43
44
45
46
47
48
49
50
51
52
53
54
55
56
57
58
59
60
ABSTRACT:

Monolayer transition-metal dichalcogenides (TMDCs) in the 2H-phase are semiconductors promising for opto-valleytronic and opto-spintronic applications because of their strong spin-valley coupling. Here we report detailed studies of opto-valleytronic properties of heterogeneous domains in CVD-grown monolayer WS_2 single crystals. By illuminating WS_2 with off-resonance circularly-polarized light and measuring the resulting spatially resolved circularly-polarized emission (P_{circ}), we find significantly large circular polarization (P_{circ} up to 60% and 45% for α - and β -domains, respectively) already at 300 K, which increases to nearly 90% in the α -domains at 80 K. Studies of spatially resolved

1
2
3 photoluminescence (PL) spectroscopy, Raman spectroscopy, x-ray photoelectron
4
5
6
7 spectroscopy (XPS), Kelvin-probe force microscopy (KPFM) and conductive atomic force
8
9
10 microscopy (CAFM) reveal direct correlation among the PL intensity, defect densities and
11
12
13 chemical potential, with the α -domains showing lower defect densities and a smaller work
14
15
16 function by 0.13 eV than the β -domains. This work function difference indicates the
17
18
19 occurrence of type-two band alignments between the α - and β -domains. We adapt a
20
21
22 classical model to explain how electronically active defects may serve as non-radiative
23
24
25 recombination centers, and find good agreement between experiments and the model.
26
27
28
29
30
31 Scanning tunneling microscopic/spectroscopic (STM/STS) studies provide further
32
33
34 evidences for tungsten vacancies (WVs) being the primary defects responsible for the
35
36
37 suppressed PL and circular polarization in WS_2 . These results therefore suggest a
38
39
40 pathway to control the opto-valleytronic properties of TMDCs *via* defect engineering.
41
42
43
44
45
46

47 KEYWORDS: transition metal dichalcogenides, WS_2 , CVD, KPFM, CAFM, STM, valley
48
49
50 polarization
51
52
53
54
55
56
57
58
59
60

1
2
3
4 There has been a surge of intense research efforts on two-dimensional (2D) van der
5
6
7 Waals (vdW) materials because of their interesting properties and great promise for
8
9
10 technological applications.¹⁻⁴ These 2D materials, such as semi-metallic graphene,⁵⁻⁹
11
12
13 insulating h-BN,¹⁰⁻¹⁴ and semiconducting transition metal dichalcogenides (TMDCs),¹⁵⁻¹⁹
14
15
16 can be synthesized on a wafer scale by chemical vapor deposition (CVD), which provides
17
18
19 a feasible route towards practical applications. The electrical and optical properties of
20
21
22 TMDCs can be significantly affected by crystal imperfections such as vacancies,
23
24
25 impurities and grain boundaries.²⁰⁻²² In particular, vacancies in TMDCs appear to be
26
27
28 unpreventable and are naturally formed inside the single crystalline grains during the CVD
29
30
31 growth process. Such vacancies can be primary contributors to carrier scattering, doping
32
33
34 effects and varying optical properties in these materials.
35
36
37
38
39
40

41
42 Among TMDCs in the 2H-phase, monolayer tungsten disulfide (WS_2) consists of a plane
43
44
45 of tungsten atoms sandwiched between top and bottom sulfur layers. It has been found
46
47
48 that atomic vacancies of tungsten and sulfur are common occurrences in WS_2 , and that
49
50
51 the electrical and optical properties of a given WS_2 monolayer are dominated by the type
52
53
54 of vacancies because of differences in the defect states. For instance, monolayer
55
56
57
58
59
60

1
2
3 hexagonal-shape WS₂ (h-WS₂) flakes with triangular heterogeneous defect domains have
4
5
6
7 been synthesized by CVD under hydrogen-rich growth conditions, as reported by several
8
9
10 research groups.²³⁻²⁷ Curiously, the optical emission in the h-WS₂ flakes exhibits
11
12
13 alternating areas of bright and dark photoluminescence (PL) emission within each h-WS₂
14
15
16 flake, and the resulting PL image looks similar to the radioactive hazard symbol, as
17
18
19 exemplified by the left panel of Figure 1a. According to previous studies,²³⁻²⁷ the α -
20
21
22 domains with a stronger PL intensity and higher mobility are associated with W-edges
23
24
25 and S-vacancies (SVs), and the β -domains with a significantly quenched PL intensity and
26
27
28 lower electron mobility exhibit a blue-shifted PL peak position, and are associated with S-
29
30
31 edges and W-vacancies (WVs). A schematic illustration of the heterogeneous defect
32
33
34 domains for WVs and SVs in a single crystalline h-WS₂ is shown in the right panel of
35
36
37
38
39
40
41
42 Figure 1a.

43
44
45 Similar to other monolayer TMDCs in the 2H-phase, monolayer WS₂ is an ideal
46
47
48 candidate for valleytronic applications due to its inequivalent K and K' valleys at the edge
49
50
51 of the Brillouin zone.²⁸⁻²⁹ Because of strong spin-orbit coupling and time-reversal
52
53
54 symmetry, the valence bands (VB) in the K (K') valley have a large energy spin splitting
55
56
57
58
59
60

1
2
3 of ~ 420 meV for WS_2 ²⁸⁻²⁹ between the top spin-up (spin-down) band and the bottom spin-
4
5
6
7 down (spin-up) band. This difference results in valley-dependent optical selection rules:
8
9
10 circularly polarized light with positive helicity ($\sigma+$) couples to the K valley and the negative
11
12
13 helicity ($\sigma-$) couples to the K' valley.³⁰⁻³² It is therefore possible to selectively populate
14
15
16
17 and manipulate the different valleys (K or K') by means of circularly polarized light.
18
19
20

21 When monolayer WS_2 is illuminated with circularly polarized light of photon energies
22
23
24 larger than the energy gap, excitons (*i.e.*, bound electron-hole pairs) are created in a
25
26
27 single valley. The radiative decay of excitons within this valley subsequently generates
28
29
30
31 circularly polarized light due to the optical selection rules. Therefore, measuring the
32
33
34 circular polarization of photoluminescence (PL) provides a direct means to monitor the
35
36
37 valley population. Valley populations will also be affected by intervalley scattering, a
38
39
40
41 process that may be enabled by Coulomb interactions or impurity/phonon scattering.³³⁻³⁶
42
43
44

45 At high temperatures or under a sufficiently high photon-excitation energy, large phonon
46
47
48 populations will couple to the valleys, thereby reducing the valley specific populations. To
49
50
51
52 date, most reports of circularly polarized PL spectra³⁷⁻⁴¹ have only been observed in
53
54
55
56
57
58
59
60

1
2
3 systems measured at relatively low temperatures (< 30 K) or near the resonant excitation
4
5
6
7 condition.
8
9

10 Here we report successful CVD growth (Figure S1) of monolayer h-WS₂ that exhibits
11
12 significant circular polarization already at room temperature and nearly 90% circular
13
14 polarization (CP) in the α -domains at 80 K without the resonant excitation condition.
15
16
17
18

19 Detailed characterizations by Raman spectroscopy, PL, X-ray photoemission
20
21 spectroscopy (XPS) and conducting atomic force microscopy (CAFM) revealed that these
22
23
24
25

26 h-WS₂ samples were of high quality, large domains and low defect densities. Additionally,
27
28 systematic studies of monolayer h-WS₂ by spatially resolved PL maps and point spectra
29
30
31
32

33 of polarized PL emission were made on the α - and β -domains of h-WS₂ at both room
34
35 temperature and low temperature (80K). We found that at room temperature, the PL
36
37
38
39

40 spectra of neutral excitons exhibited a CP of $\sim 50\%$ and $\sim 40\%$ in the α - and β -domains,
41
42
43
44
45 respectively. Moreover, the degree of circularly polarized emission in α -domains
46
47
48

49 approached $\sim 90\%$ at 80K, suggesting nearly perfect valley polarization. Spatially-
50
51
52 resolved CAFM studies revealed that the areal defect density was on the order of 10^{10}
53
54

55 cm⁻² in the α -domains and on the order of 10^{11} cm⁻² in the β -domains. Following a similar
56
57
58
59
60

1
2
3 analysis in Refs. 42 and 51, we related the areal defect density in each domain to the
4
5
6
7 corresponding PL intensity and obtained an estimate for the non-radiative recombination
8
9
10 lifetime.^{42,51} Additionally, spatially resolved studies using Kelvin-probe force microscopy
11
12
13 (KPFM) found that the work function in the β -domains was consistently larger than that in
14
15
16 the α -domains by 0.15 eV, suggesting type-2 semiconducting band alignments along the
17
18
19 domain boundaries that are favorable for stabilizing interfacial excitons.⁵² Atomically
20
21
22 resolved imaging and spectroscopic studies by scanning tunneling microscopy (STM)
23
24
25 further revealed that the non-radiative defects were primarily associated with the WVs
26
27
28 rather than SVs, consistent with the CAFM findings in regions of higher defect densities.
29
30
31
32
33
34
35 Our results thus provide direct evidences for WVs being the primary non-radiative
36
37
38 recombination sites in h-WS₂ that are responsible for the suppression of PL intensity and
39
40
41 circular polarization.
42
43
44

45 RESULTS AND DISCUSSION

46
47
48

49 Monolayer h-WS₂ samples were synthesized on SiO₂ (300 nm)/Si substrates by means
50
51
52 of CVD, as schematically shown in Figures S1 and S2. The hexagonal flakes typically
53
54
55 had lateral dimensions on the order of several tens to hundreds of micrometers so that
56
57
58
59
60

1
2
3 optical studies at many discrete locations across a single flake could be carried out.
4
5

6
7 Further details for the h-WS₂ growth processes are described in Methods and
8
9
10 Supplementary Information Note 1.
11
12

13
14 Our monolayer h-WS₂ samples exhibited typical fluorescence images analogous to the
15
16
17 radioactive hazard symbol, as mentioned in the introduction and exemplified in Figure 1a.
18
19

20
21 Spatially resolved topographic studies on the same samples using atomic force
22
23
24 microscopy (AFM) revealed smooth topographic maps (Figure 1b). Specifically, while the
25
26

27
28 height difference between the WS₂ single crystal and the SiO₂/Si substrate was ~ 0.85
29
30
31 nm, which was consistent with the monolayer thickness of WS₂, there was no discernible
32
33

34
35 height differences between the two domains of different PL intensities (Figure 1d).
36
37
38 Spatially resolved measurements of the AFM phase mode revealed a clear phase
39
40

41
42 difference (1°) between the two domains (Figure 1c), and the resulting phase map
43
44
45 correlated well with the pattern shown in Figure 1d. Similarly, spatially resolved Raman
46
47

48
49 spectroscopic maps for the A_{1g} and E_{2g}^1 modes of a monolayer h-WS₂ single crystal
50
51
52 (shown respectively in Figures 1e and 1f) also exhibited the same pattern.
53
54
55
56
57
58
59
60

1
2
3
4 Figure 1g shows a representative PL spectrum from 1.96 eV to 2.01eV for the typical
5
6
7 A-exciton peak of h-WS₂. The A-exciton PL peak for the α -domain is redshifted compared
8
9
10 to that of the β -domain. This redshift may be attributed to tensile strain existed in the α -
11
12
13 domains and/or to a higher carrier density. Moreover, the PL intensity in the α -domains
14
15
16 is always enhanced by about one order of magnitude when compared with the β -domains.
17
18
19
20

21 Generally speaking, the PL intensity can be modulated by a variety of factors such as
22
23
24 stoichiometry, strain, doping and density of non-radiative recombination centers. To
25
26
27 investigate the contributions from strain and doping effects, we performed Raman
28
29
30 intensity and frequency mapping of the A_{1g} and E_{2g}¹ modes, which displayed contrast
31
32
33 between the α - and β -domains (Figures 1e-f) and were similar to the PL mapping (Figure
34
35
36 1d). We found that the strain-related E_{2g}¹ mode exhibited a redshift in the α -domain relative
37
38
39 to the β -domain (0.5 cm⁻¹), indicating a tensile-strain effect. Similarly, the redshift (1.2 cm⁻¹
40
41
42 1) of the doping-related A_{1g} mode in the α -domain relative to the β -domain implied carrier
43
44
45 doping effects (Figure 1h), which was consistent with the observed PL redshift (Figure
46
47
48
49 1g). The LA (M) mode at 176 cm⁻¹, which is associated with the longitudinal acoustic
50
51
52
53
54
55
56
57
58
59
60

1
2
3
4 phonon at the M point of the Brillouin zone, may be considered as a useful indicator of
5
6
7 the sample quality. Specifically, a finite intensity of the LA (M) mode implies the presence
8
9
10 of defects or disorder that satisfied the $q = 0$ Raman selection rule. Additionally, the
11
12
13 intensity of the LA (M) mode, $I(\text{LA})$, may be related to the inter-defect spacing (L_D)⁴³ by
14
15
16 the expression $I(\text{LA}) \propto L_D^{-2}$. Figure S3 demonstrates that the intensity of the LA (M) mode
17
18
19 associated with the β -domain was shown to be larger than that of the α -domain, implying
20
21
22 a shorter inter-defect distance and therefore a higher areal density of disorder in the β -
23
24
25 domain that signifies more non-radiative recombination centers and a reduced PL
26
27
28 intensity.
29
30
31
32
33
34

35 In addition to the PL/Raman spectroscopic studies, spatially-resolved X-ray
36
37
38 photoelectron emission spectroscopy (XPS) was carried out on monolayer WS₂
39
40
41 transferred to Au (111) / mica substrates (Figure 2a) to probe the chemical composition
42
43
44 and stoichiometry of the h-WS₂ single crystal. High-resolution XPS mapping performed
45
46
47 on the h-WS₂ samples revealed apparent hexagonal geometry, as exemplified in Figure
48
49
50 S4a. Photoelectrons from core level of W and S atoms were acquired from both α - and
51
52
53
54
55
56
57
58
59
60

1
2
3
4 β -domains. As shown in Figures 2b and 2c, the corresponding binding energies in the α -
5
6
7 domain (β -domain) were 34.31 eV (34.44 eV) for $W_{4f\ 5/2}$, 32.15 eV (32.28 eV) for $W_{4f\ 7/2}$,
8
9
10 162.87 eV (162.9 eV) for $S_{2p3/2}$, and 163.07 eV (163.1 eV) for $S_{2p1/2}$. Considering the error
11
12
13 range of ± 0.025 eV for the binding energies determined using our XPS system, the upshift
14
15
16 in the α -domain binding energies (~ 0.13 eV) relative to those in the β -domain was
17
18
19 prominent for the W-4f peaks, in good agreement with the valence-band maximum shift
20
21
22 due to doping-induced Fermi level modulation. In contrast, the upshift of the S-2p peaks
23
24
25 (~ 0.03 eV) was much smaller and essentially negligible given the error range of our XPS
26
27
28 system. This negligible upshift of the S-2p peaks in the α -domain may be attributed to the
29
30
31 tensile strain effect that affected the S-2p valence electrons more significantly, which
32
33
34 contributed to a binding-energy downshift that compensated the doping-induced binding
35
36
37 energy upshift. On the other hand, the tensile strain had much weaker effects on the W-
38
39
40 4f core electrons so that the doping-induced energy upshifts prevailed for the W-4f peaks
41
42
43 in the α -domain.
44
45
46
47
48
49
50
51

52 We have also explored the surface potential (work function) of the α - and β -domains
53
54
55 *via* Kelvin probe force microscopy (KPFM) because the work functions of semiconductor
56
57
58
59
60

1
2
3
4 2D materials are sensitive to the corresponding variable Fermi level. To determine the
5
6
7 work function of the Al-coated AFM tip, we first performed UPS measurements on the Au
8
9
10 (111) / mica sample, which found the work function of Au (111) to be 4.8 eV, as shown in
11
12
13
14 Figure S4b. Next, we performed KPFM measurements using the Al-coated AFM tip on
15
16
17 Au (111) / mica, which yielded the value of the contact potential difference (V_{CPD}^0) between
18
19
20 the Al-coated AFM tip and Au (111), where the contact potential difference (V_{CPD}^0) was
21
22
23 defined as the difference between the work function of the tip (ϕ_{tip}) and that of Au (111),
24
25
26 so that $eV_{\text{CPD}}^0 = \phi_{\text{tip}} - 4.8 \text{ eV}$. Finally, KPFM measurements using the Al-coated AFM tip on
27
28
29 h-WS₂ yielded the contact potential difference (V_{CPD}) between the Al-coated AFM tip and
30
31
32 different domains of the h-WS₂ sample so that we obtained the following relation:
33
34
35
36
37

$$eV_{\text{CPD}} = \phi_{\text{tip}} - \phi_{\text{WS}_2}, \Rightarrow \phi_{\text{WS}_2} = \phi_{\text{tip}} - eV_{\text{CPD}}, \quad (1)$$

38
39
40
41 where ϕ_{WS_2} is the work function of the WS₂ sample. From spatially resolved
42
43
44 measurements of V_{CPD} , the work function difference between the α - and β -domains can
45
46
47 be determined, and the resulting KPFM images are shown in Figures 2d and 2e.
48
49
50
51
52
53
54
55
56
57
58
59
60

1
2
3 A schematic representation of the band diagram with the Fermi levels for the α - and β -
4 domains relative to the vacuum level is shown in Figure 2f. The difference in the Fermi
5
6
7 domains relative to the vacuum level is shown in Figure 2f. The difference in the Fermi
8
9
10 levels between the α - and β -domains can be calculated directly from V_{CPD} using the
11
12
13 following equation:
14
15

$$\Delta E_f = E_{f,\alpha} - E_{f,\beta} = eV_{\text{CPD},\alpha} - eV_{\text{CPD},\beta} = e\Delta V_{\text{CPD}} = (\phi_\beta - \phi_\alpha), \quad (2)$$

16
17
18 where $E_{f,\alpha}(\phi_\alpha)$ and $E_{f,\beta}(\phi_\beta)$ are the Fermi levels (work functions) of the α - and β -
19
20
21 domains, respectively. Interestingly, we note that the band diagram at the interface of the
22
23
24
25
26
27
28 α - and β -domains is consistent with a type-2 band alignment that supports long-lived
29
30
31 interfacial excitons.⁵²
32
33

34
35 To investigate the degree of valley polarization in our monolayer h-WS₂, we performed
36
37
38 polarization-resolved PL spectroscopy measurements at both room temperature and 80
39
40
41 K under the excitation of a 514 nm continuous-wave laser source, as schematically
42
43
44
45 illustrated in Figure 3a.
46
47

48
49 For spatially-resolved PL mapping, the sample was excited with σ_+ helicity and the laser
50
51
52 was scanned across a (13 $\mu\text{m} \times 13 \mu\text{m}$) area at a step size of 0.2 μm . The detection optics
53
54
55
56
57
58
59
60

1
2
3 were set first for the σ_+ analysis and then for the σ_- analysis over the same area in two
4
5
6
7 separate scans. The energy of the PL peak within the range of 1.9 eV to 2.1 eV for the
8
9
10 σ_+ (σ_-) detection was determined, and the PL intensity map taken at the peak energy is
11
12
13
14 shown in Figure 3b for the σ_+ detection and in Figure 3c for the σ_- detection, both obtained
15
16
17 at room temperature (RT). These PL maps reveal the same emission pattern as the
18
19
20 unpolarized excitation. This type of PL pattern, with lower PL intensity in the β -domain
21
22
23 and higher PL intensity in the α -domain (about 10 times stronger than that in the β -
24
25
26 domain), was common among all monolayer h-WS₂ single crystals that we synthesized.
27
28
29
30

31 Given the polarization-resolved PL intensities $I(\sigma_+)$ and $I(\sigma_-)$, the degree of circular
32
33
34 polarization (P_{circ}) is define by the following expression:
35
36
37

$$P_{\text{circ}} = \frac{I(\sigma_+) - I(\sigma_-)}{I(\sigma_+) + I(\sigma_-)}. \quad (3)$$

38
39
40
41
42
43 Using Eq. (3), the degree of circular polarization across a monolayer h-WS₂ crystal was
44
45
46 obtained and is illustrated in Figure 3d. The higher degree of polarization (DOP) in the α -
47
48
49 domain (45% ~ 60%) and lower DOP in the β -domain (20% ~ 45%) was found to be well
50
51
52
53
54
55
56
57
58
59
60

1
2
3 correlated to the PL intensity pattern. Similar results were also obtained for polarization-
4
5
6
7 resolved mapping acquired with the σ_- excitation, as shown in Figure S5.
8
9

10 The PL spectra of the α -domain (Figure 3e) and the β -domain (Figure 3f) taken at RT
11
12 both displayed a single peak with the maximum intensity at 1.92 eV, indicating that the
13
14
15
16
17 RT emission characteristics were dominated by the neutral excitons. These neutral
18
19
20
21 excitons exhibited very large circular polarization at both the α -domain ($P_{circ} \sim 50\%$) and
22
23
24
25 β -domain ($P_{circ} \sim 40\%$) of our h-WS₂ samples even at RT, in stark contrast to recent
26
27
28 reports by other groups (with $P_{circ} = 0.2\% \sim 32\%$) on monolayer WS₂,⁴⁰⁻⁴² as summarized
29
30
31 in Table S2. The PL peak for both domains was found to slightly blue-shift to 1.96 eV at
32
33
34
35 a lower temperature (LT) 80 K. As exemplified in Figure 3g, the LT (80 K) PL intensity of
36
37
38 the σ_+ detection at the α -domain increased threefold relative to the corresponding RT
39
40
41 signals, whereas the PL intensity of the σ_- detection remained the same at 80 K. In
42
43
44 particular, the DOP at the α -domain approached nearly 90% at 80 K. In contrast, the LT
45
46
47
48 (80K) PL spectra at the β -domain revealed that the PL intensities for both the σ_+ and σ_-
49
50
51
52 detections increased tenfold relative to the corresponding PL spectra at RT, as
53
54
55
56
57
58
59
60

1
2
3 exemplified by Figure 3h. However, the DOP of the β -domain at 80 K remained largely
4
5
6
7 the same as that at RT.
8
9

10 Our finding of significant disparity in the DOP enhancement with decreasing
11
12
13
14 temperature for two different domains is quite unusual: while the common observation of
15
16
17 increasing PL intensity with decreasing temperature may be attributed to the reduction of
18
19
20 thermally activated non-radiative recombination, this mechanism should have resulted in
21
22
23 a comparable enhancement factor with decreasing temperature for the PL intensity in the
24
25
26
27 same material. However, the enhancement factor for the PL intensity at LT was
28
29
30 apparently different in different domains of the h-WS₂ single crystal, which led to
31
32
33 significantly different DOP at LT. A feasible explanation for such disparity in the DOP
34
35
36 enhancement with decreasing temperature may be due to negligible non-radiative
37
38
39 recombination centers for excitons in the α -domain as opposed to more non-radiative
40
41
42 recombination centers in the β -domain. To shed light on this issue, we performed
43
44
45 spatially-resolved conductive atomic force microscope (CAFM) measurements to be
46
47
48
49
50
51
52 detailed below, which facilitated precise identifications of defects that could serve as the
53
54
55
56
57
58
59
60

1
2
3 non-radiative recombination centers and also provided direct quantifications of the areal
4
5
6
7 defect density.
8
9

10 A schematic illustration of the experimental configuration for the conductive atomic force
11
12
13
14 microscope (CAFM) measurements is shown in Figure 4a, where all data acquisition was
15
16
17 done at RT in air. It is worth noting that careful sample preparation for the CAFM
18
19
20 measurements was critically important to obtaining reproducible results. In particular, an
21
22
23 atomically flat conductive substrate for the monolayer h-WS₂ sample was necessary. For
24
25
26 this purpose, we first transferred a thick piece of CVD-grown graphite onto an atomically
27
28
29 flat Au (111) (200 nm) / mica substrate, followed by a monolayer of h-WS₂ transferred
30
31
32 from its CVD growth substrate onto the graphite/Au (111)/mica substrate. After the
33
34
35 transfer, we annealed the combined sample-on-substrate in a hydrogen-argon gas
36
37
38 mixture (with a ratio of H₂ to Ar of 1 to 3) for 3 hours to remove possible contaminants
39
40
41 and wrinkles, which helped improve the contact uniformity between the monolayer h-WS₂
42
43
44 and the graphite substrate. Details of the h-WS₂ transfer and the annealing processes
45
46
47
48 can be found in Methods and Supplementary Information. Lastly, a voltage was applied
49
50
51 to the sample lead so that a current flowed between the Pt/Ir coated CAFM tip and the
52
53
54
55
56
57
58
59
60

1
2
3
4 sample, and this current was recorded by a current amplifier. By scanning the AFM tip
5
6
7 across the sample and recording the currents at each pixel with a pixel spacing of 0.9 nm,
8
9
10 we obtained spatially resolved CAFM maps over different domains of the h-WS₂ sample.
11
12
13

14 In these CAFM maps, the locations of defects were easily identified as distinct high-
15
16
17 current features: the defect locations generally exhibited more than 2 orders of magnitude
18
19
20 higher currents than areas without defects. Additionally, the electrical characteristics of
21
22
23 each defect could be well quantified by measurements of the current-voltage (I-V) curves,
24
25
26 as exemplified in Figure 4b by the comparison of a typical I-V curve obtained on a defect
27
28
29 with a reference I-V curve obtained away from any defects. The I-V curve associated with
30
31
32 a defect exhibited much enhanced currents at bias voltages $|V| > 0.3$ V and was nearly
33
34
35 symmetric about zero applied bias. These defect sites were generally much more
36
37
38 conductive than regions without defects, as demonstrated by the comparison of the
39
40
41 differential conductance taken on and off defects in the inset of Figure 4b.
42
43
44
45
46
47
48

49 In Figures 4d-i, spatially-resolved CAFM differential conductance maps taken at a bias
50
51
52 voltage of 0.9 V are shown over different 1 μm \times 1 μm areas at locations specified on the
53
54
55 h-WS₂ single crystal in Figure 4c, which shows a spatial map of PL intensity taken on the
56
57
58
59
60

1
2
3 sample after its transfer onto the substrate for the CAFM measurements. The apparent
4
5
6
7 visibility of defect locations in the CAFM maps enabled direct counting of the number of
8
9
10 the defects in both the α - and β -domains. Specifically, for the α -domain, we found 149
11
12
13 defects in Figure 4d, which corresponded to a defect density of $1.49 \times 10^{10} \text{ cm}^{-2}$. Similarly,
14
15
16 we obtained 175 defects ($1.75 \times 10^{10} \text{ cm}^{-2}$) in Figure 4e, and 359 defects ($3.59 \times 10^{10} \text{ cm}^{-2}$)
17
18
19 in Figure 4f. For the β -domain, we found 822 defects ($8.22 \times 10^{10} \text{ cm}^{-2}$) in Figure 4g, 1370
20
21
22 defects ($1.37 \times 10^{11} \text{ cm}^{-2}$) in Figure 4h, and 1750 defects ($1.75 \times 10^{11} \text{ cm}^{-2}$) in Figure 4i.
23
24
25
26
27
28 These CAFM measurements clearly indicated that the areal density of these highly
29
30
31
32
33
34
35
36
37
38
39
40
41
42
43
44
45
46
47
48
49
50
51
52
53
54
55
56
57
58
59
60

the α -domain.

Here we emphasize that other types of defects not detectable by the CAFM measurements may exist, and in this work we only consider one specific type of defects that are most electrically active and correlate their densities with the corresponding spatially-resolved PL. In Figure 4j we compare the defect density and the PL intensity as a function of the position numerated along a line in Figure 4c, and find that the measured defect density generally anti-correlates with the PL intensity for both α - and β -domains.

1
2
3 A major challenge to understanding the excitonic behavior in h-WS₂ is the wide variety
4
5
6
7 of mechanisms that can affect the exciton recombination, including substrate effects,
8
9
10 defect related recombination and other non-radiative recombination pathways⁴⁴⁻⁵¹. From
11
12
13
14 our experiments, the apparent anti-correlation between the defect density and the PL
15
16
17 intensity is helpful in identifying the role of defects in the exciton recombination for
18
19
20
21 monolayer h-WS₂.

22
23
24 Generally speaking, the PL intensity is proportional to the PL quantum yield (QY) of
25
26
27 excitons, and a standard QY is defined by the following expression:

$$\text{QY} \equiv \tau_r^{-1} / (\tau_r^{-1} + \tau_{nr}^{-1}), \quad (4)$$

34
35 where τ_r (τ_{nr}) is the average radiative (non-radiative) recombination time of excitons.

36
37
38 Typically the non-radiative recombination rate τ_{nr}^{-1} may be further divided into two
39
40
41
42 components if we assume that excitons do not interact with each other. That is,

$$\tau_{nr}^{-1} = \tau_{nr,sub}^{-1} + \tau_{nr,defect}^{-1}, \quad (5)$$

1
2
3 where $\tau_{nr,sub}$ is the average non-radiative recombination time for substrate related effects,
4
5
6
7 which may also include any other non-radiative recombination mechanisms, and $\tau_{nr,defect}$
8
9
10 is the average non-radiative recombination time for defect-related effects.
11
12
13

14 To understand the correlation between the defect density and PL intensity, we followed
15
16
17 a similar analysis by Rosenberger *et al.*⁴² Specifically, we assumed that the defect-related
18
19
20 non-radiative recombination occurred when excitons collided with defects and resulted in
21
22
23 non-radiative recombination. For an exciton with an effective collision radius r traveling
24
25
26 with a speed v , an area swept by the exciton over a time period t in the 2D sheet with a
27
28
29 defect density n_d would result in N collisions, where $N = n_d(2rvt)$. Therefore, the collision
30
31
32 time $\tau_{nr,defect}$ between the exciton and defects can be defined by the following expression:
33
34
35
36
37

$$38 \tau_{nr,defect} = \frac{t}{N} = \frac{t}{n_d(2rvt)} = \frac{1}{2rvn_d}, \Rightarrow \tau_{nr,defect}^{-1} = 2rvn_d. \quad (6)$$

39
40
41
42
43 Combining Eqs. (4)-(6) and assuming that the QY and the empirical PL intensity, $(PL)_{exp}$,
44
45
46 are related by a scaling coefficient C , we arrived at the following relation:⁴²
47
48
49

$$50 (PL)_{exp} = C \frac{\tau_r^{-1}}{\tau_r^{-1} + \tau_{nr,sub}^{-1} + 2rvn_d}. \quad (7)$$

1
2
3
4 Empirically, the values of τ_r in different domains could be directly determined from time
5
6
7 resolved PL (TRPL), which yielded $\tau_r = 1.5$ ns in the α -domain and $\tau_r = 230$ ps in the β -
8
9
10 domain for monolayer h-WS₂. These values were consistent with the range of 0.2 ~ 4 ns
11
12
13 reported in the literature for monolayer WS₂.^{43,48,50} If we further assumed that a thermal
14
15
16 speed of excitons at room temperature (RT) of $v = 10^5$ m/s,^{53,54} and an effective collision
17
18
19 radius $r = 2.1$ nm based on previous reports,⁵⁴ we obtained in Figure 4k the relation
20
21
22 between the spatially varying PL intensity of a monolayer h-WS₂ on graphite/Au
23
24
25 (111)/mica and the corresponding local defect density. The solid black line represents the
26
27
28 fitting curve for the PL measurements using Eq. (7) with the fitting parameters $C = 3.1 \times 10^5$
29
30
31 and $\tau_{nr,sub} = 30$ ps. These fitting parameters were consistent for both domains in h-WS₂,
32
33
34
35 which implies that our direct quantification of the defect density n_d helped decouple the
36
37
38 defect-related non-radiative recombination (associated with $\tau_{nr,defect}^{-1} = 2rvn_d$) from other
39
40
41 non-radiative mechanisms (associated with $\tau_{nr,sub}^{-1}$).

42
43
44
45
46
47
48
49 To understand why the DOP differed in the α - and β -domains, we considered a rate
50
51
52 equation model in the steady state to find the relationship between the DOP and defect-
53
54
55
56
57
58
59
60

1
2
3 related non-radiative recombination. As detailed in Supplementary Information Note 6,
4
5
6
7 the circular polarization P_{circ} for neutral excitons in the steady-state rate model can be
8
9
10 given by the following expression:

$$P_{circ} = \frac{P_0(1-\delta)^2}{1+2(\tau_{ex}/\tau_{intervalley})} = \frac{P_0 \left[1 - (\delta_{imp} + \delta_{phonon})^2 \right]}{1+2(\tau_{ex}/\tau_{intervalley})}, \quad (8)$$

11
12
13
14
15
16
17
18
19 where P_0 is the theoretical degree of circular polarization, τ_{ex} ($\tau_{intervalley}$) is the neutral
20
21
22 exciton (intervalley) relaxation time, and $(1-\delta)$ represents the selectivity in the initial
23
24
25
26
27 excitation with $0 < \delta < 1$.³² In particular, we may express $\delta = \delta_{imp} + \delta_{phonon}$ to account for
28
29
30 impurity/defects/substrate-related and phonon-assisted recombination effects that led to
31
32
33
34 inter-valley mixing from finite-momentum scattering,³² with $(1-\delta)$ decreasing with
35
36
37 increasing scattering densities and increasing temperature. Thus, from Eq. (8) we expect
38
39
40
41 P_{circ} to increase with either decrease in τ_{ex} , increase in $\tau_{intervalley}$, or decrease in δ . For both
42
43
44 α - and β -domains of the same h-WS₂ sample, given that they were excited with the same
45
46
47 laser power and wavelength, and were also exposed to the same ambient, we may
48
49
50
51 assume that the optically generated exciton densities n_K^{ex} and $n_{K'}^{ex}$ were the same for both
52
53
54
55 domains.
56
57
58
59
60

1
2
3
4 In monolayer TMDCs at RT, the non-radiative lifetimes may be several orders of
5
6
7 magnitude shorter than the radiative lifetime so that the overall exciton lifetime is much
8
9
10 reduced. From our CAFM measurements at RT and using Eqs. (6) – (7) to fit the PL
11
12
13 intensities, we found that the α -domains with lower defect densities would exhibit higher
14
15
16 PL intensities and longer non-radiative lifetimes ($\tau_{nr} = 4.7 \text{ ps} \sim 10 \text{ ps}$ for $n_d = 3.59 \times 10^{10}$
17
18 $\text{cm}^{-2} \sim 1.49 \times 10^{10} \text{ cm}^{-2}$), whereas the β -domains with higher defect densities would exhibit
19
20
21 lower PL intensities and shorter non-radiative lifetimes ($\tau_{nr} = 1.1 \text{ ps} \sim 2.6 \text{ ps}$ for $n_d =$
22
23
24 $1.75 \times 10^{11} \text{ cm}^{-2} \sim 8.22 \times 10^{10} \text{ cm}^{-2}$). By considering the radiative (τ_r) and non-radiative (τ_{nr})
25
26
27 lifetimes of excitons in both domains, we could directly estimate the exciton lifetime τ_{ex}
28
29
30 by the relation $\tau_{ex}^{-1} = \tau_r^{-1} + \tau_{nr}^{-1}$, which yielded larger values of $\tau_{ex} = 4.72 \text{ ps} \sim 10 \text{ ps}$ for the
31
32
33 α -domains and smaller values of $\tau_{ex} = 1.1 \text{ ps} \sim 2.6 \text{ ps}$ for the β -domains at RT.
34
35
36
37
38
39
40
41
42 Additionally, the large differences in the defect density between the α - and β -domains
43
44
45 gave rise to lower selectivity (*i.e.*, smaller $(1-\delta)^2$) in the β -domains. Therefore, the nearly
46
47
48 temperature independent P_{circ} in the β -domain may be understood in terms of the
49
50
51 competing effects between increasing $(1-\delta)^2$ and decreasing $(\tau_{ex})^{-1}$ with decreasing
52
53
54
55
56
57
58
59
60

1
2
3 temperature according to Eq. (8). In contrast to the β -domain, $(\tau_{ex})^{-1}$ in the α -domain did
4
5
6
7 not decrease as much with decreasing temperature due to far fewer non-radiative
8
9
10 recombination sites, whereas the selectivity $(1-\delta)^2$ increased more significantly with
11
12
13 decreasing temperature due to diminishing δ_{phonon} and negligible δ_{imp} . Therefore, the value
14
15
16
17 of P_{circ} increased dramatically with decreasing temperature in the α -domains according
18
19
20
21 to Eq. (8), consistent with our experimental finding.
22
23

24 While the temperature-dependent PL intensities and DOP in both the α - and β -domains
25
26
27 of h-WS₂ can be consistently explained in terms of the differences in the density of
28
29
30 electrically-active defects, the microscopic origin for these defects is not yet understood.
31
32
33
34 By performing scanning tunneling microscopy (STM) measurement on monolayer WS₂
35
36
37 single crystals,^{55,56} we obtained atomically spatial-resolved images associated with either
38
39
40
41 the SVs (Figure 5a) or the WVs (Figure 5d).
42
43
44

45 For the SV sites of WS₂, as exemplified by the white dash triangles in Figure 5a, the
46
47
48 corresponding tunneling conductance spectra were found to be comparable to those of
49
50
51 vacancy-free regions. Specifically, both the tunneling current (I) vs. bias voltage (V)
52
53
54 spectra and the corresponding (dI/dV) -vs.- V spectra taken at a SV (represented by the
55
56
57
58
59
60

1
2
3 red curves in Figures 5b and 5c for the SV location $\alpha 1$ shown in Figure 5a) is essentially
4
5
6 indistinguishable from those taken at a vacancy-free region (represented by the orange
7
8
9 curves in Figures 5b and 5c for the vacancy-free location $\alpha 2$ shown in Figure 5a). In
10
11
12 particular, the (dI/dV) spectra revealed that the valence band maximum (VBM) and
13
14
15 conduction band minimum (CBM) were located at $E_{\text{VBM}} \sim -1.1$ eV and $E_{\text{CBM}} \sim +0.9$ eV,
16
17
18 respectively, yielding a band gap of $E_g = E_{\text{CBM}} - E_{\text{VBM}} = \sim 2$ eV (Figure 5c). In contrast, for
19
20
21 the WV sites as exemplified by the large white dashed triangle in the Figure 5d, the
22
23
24 tunneling spectra taken at the WV sites β_1 and β_2 , respectively illustrated by the blue and
25
26
27 green curves in Figure 5e for the I -vs.- V spectra and in Figure 5f for the (dI/dV) -vs.- V
28
29
30 spectra, revealed an enhance differential conductance at smaller biased voltages and a
31
32
33 smaller bandgap of ~ 1.1 eV, with the VBM and CBM move to ~ -0.8 eV and $\sim +0.3$ eV,
34
35
36 respectively. These spectra associated with the WVs were qualitatively similar to the
37
38
39 CAFM measurements in Figure 4b, even though direct quantitative comparison of the
40
41
42 *tunneling* conductance data from STM with the *contact* conductance data derived from
43
44
45 CAFM is not straightforward without detailed information and modeling of the nanoscale
46
47
48 interfacial properties between the AFM tip and WS_2 . Overall, the combined information
49
50
51
52
53
54
55
56
57
58
59
60

1
2
3 derived from atomically resolved STM studies and the nanoscale CAFM measurements
4
5
6
7 strongly suggests that the WV sites rather than the SV sites in monolayer WS₂ are the
8
9
10 primary non-radiative combination centers that are responsible for the reduction in the PL
11
12
13
14 intensity and DOP.
15

16
17 The aforementioned scenario of a higher WV density in the β -domain is not only
18
19
20 consistent with the observation of reduced PL intensities and DOP but also accounts for
21
22
23
24 the larger work function in the β -domain (as found by the KPFM studies) because of the
25
26
27
28 excess hole-doping associated with WVs in WS₂. Therefore, we have been able to
29
30
31 provide a unified description for the varying chemical, electronic and optical properties of
32
33
34
35 different domains in monolayer h-WS₂ in terms of the varying WV densities.
36
37

38 Finally, we note that a well-defined, net valley polarization can be established along the
39
40
41
42 boundary between the α - and β -domains under circularly polarized light as the result of
43
44
45
46 their different DOP. Hence, the domain boundaries in our monolayer h-WS₂ samples may
47
48
49 be considered as one-dimensional *topological channels* so that a Hall bar device
50
51
52 patterned along one of the domain boundaries is expected to exhibit CPL-induced valley
53
54
55
56 Hall currents even at room temperature. Such opto-valleytronic and related opto-
57
58
59
60

1
2
3 spintronic phenomena for devices fabricated along the topological channels in monolayer

4
5
6
7 h-WS₂ will be an interesting topic for future investigation.
8
9

10 11 12 CONCLUSION

13
14
15 In summary, our experimental investigations based on spatially resolved
16
17
18 measurements of PL, Raman spectroscopy, XPS, KPFM, CAFM and STM have clarified
19
20
21 the microscopic physical origin for markedly different reports of PL properties in CVD-
22
23
24 grown monolayer WS₂ by attributing the differences to varying densities of tungsten
25
26
27 vacancies (WVs) that act like non-radiative recombination centers. We have also
28
29
30 demonstrated large circular polarizations in the PL spectra of our monolayer CVD-grown
31
32
33 h-WS₂ single crystals under off-resonant illumination and at relatively high temperatures
34
35
36 (from RT to 80 K) when compared with other TMDCs, as detailed in Tables S1 and S2
37
38
39 and summarized in Figure S7. The occurrence of type-two band alignments along the
40
41
42 domain walls of h-WS₂ further promises longer exciton lifetimes along the domain
43
44
45 boundaries. This work therefore suggests a pathway towards engineering valley
46
47
48
49
50
51
52
53
54
55
56
57
58
59
60

1
2
3 polarizations and exciton lifetimes in TMDCs by controlling the type and density of defects
4
5
6

7 that serve as non-radiative exciton recombination sites.
8
9
10
11
12
13
14
15
16
17
18
19
20
21
22
23
24
25
26
27
28
29
30
31
32
33
34
35
36
37
38
39
40
41
42
43
44
45
46
47
48
49
50
51
52
53
54
55
56
57
58
59
60

METHODS

Sample preparation

Pre-treatment of SiO₂/Si substrate: SiO₂/Si substrates (300 nm SiO₂) were used for the CVD growth of WS₂. Prior to the growth, SiO₂/Si substrates were first soaked and sonicated in acetone and isopropyl alcohol (IPA) for 30 minutes to remove organic impurities, and then soaked in Nanostrip for 60 minutes, and finally washed with deionized water and dried with nitrogen gas.

Synthesis of mono- and multilayer WS₂: We used WO₃ and S as precursors in an atmospheric pressure CVD system to grow monolayer h-WS₂ on Si/SiO₂ substrates. A schematic drawing of the home-built CVD system is shown in Figure S1. Our setup includes the following parts: a quartz tube with a diameter of 1 inch and a length of 100 cm, a one-inch inner diameter (I.D.) horizontal split tube furnace (Lindberg Blue M), two mass flow controllers calibrated for Ar and H₂, with stainless steel flanges at both ends connected to a chiller water circulation system operating at 10 °C.

In the first step of the procedure, 95 mg WO₃ precursor mixed with 5mg KI was placed in a quartz boat containing the SiO₂/Si substrates set face-down directly above the W

1
2
3 source precursor, and the quartz boat was then positioned at the center of the furnace. A
4
5
6
7 second boat containing 100 mg S (Alfa Aesar, 99.999+ %) was placed upstream at 16
8
9
10 cm away from the W source. Next, the system was pump down to 3×10^{-2} torr to eliminate
11
12
13 air and moisture. After the system reached the base pressure, the Ar/H₂ (80/40 sccm)
14
15
16 carrier gas was introduced until atmospheric pressure was achieved. The furnace was
17
18
19 then heated up with a ramp rate of 35 °C/min to the growth temperatures (750 to 850 °C).
20
21
22 The Sulphur component melted at 150 °C was sent into the furnace at the growth
23
24
25 temperature to grow h-WS₂. The sample growth procedure proceeded for 10 minutes,
26
27
28 after which the furnace was directly opened to room temperature to stop the reaction
29
30
31
32 immediately.
33
34
35
36
37

38 **Transfer of mono- and multilayer WS₂:** Polystyrene (PS) was used as the supplementary
39
40
41 film to peel off the WS₂ crystals from sapphire substrates. PS (M.W. 192000) dispersed
42
43
44 in toluene solution (20 mg/mL) was spin-coated on top of the WS₂ sample at a speed of
45
46
47
48 3000 rpm. The edge of the PS film was scribed with a blade, and then the sample of PS/h-
49
50
51 WS₂/Si-substrate was inserted into water slowly. The PS/h-WS₂ film became peeled off
52
53
54 naturally in water, and was subsequently rinsed with deionized-water thrice before it was
55
56
57
58
59
60

1
2
3
4 picked up and placed onto the target substrate. The PS coating was removed with toluene
5
6
7 after baking the sample at 80°C for 60 minutes.
8
9

14 **Characterizations by atomic probe microscopy and Kelvin probe force microscopy**

15
16
17 Atomic Force Microscopy (AFM) (Bruker Dimension Icon) under the tapping mode was
18
19
20 applied to characterize the surface morphology of the WS₂ film transferred onto the
21
22
23 SiO₂/Si substrate. The Kelvin probe force microscopy (KPFM) measurements were
24
25
26
27 conducted on a Bruker Dimension Icon SPM. Doped silicon PFQNE-AL probes (Bruker)
28
29
30
31 with a probe radius of 5 nm and a spring constant of 0.8 N/m were used for the electrical
32
33
34
35 measurements.
36
37
38
39
40
41

42 **Spectroscopic characterization**

43
44
45 The quality of the WS₂ film was characterized using Raman spectroscopy, PL
46
47
48 measurements, X-ray photoemission spectroscopy (XPS), and Ultraviolet photoemission
49
50
51 spectroscopy (UPS). The Raman spectra were taken with a Renishaw M1000 and
52
53
54
55 Renishaw InVia Raman spectrometer system using a 514.3 nm laser (2.41 eV) as the
56
57
58
59
60

1
2
3 excitation source. A 50× objective lens with a numerical aperture of 0.75 and a 2400
4
5
6
7 lines/mm and 1800 lines/mm grating were chosen during the measurement to achieve
8
9
10 better signal-to-noise ratio. XPS and UPS studies were performed under ultra-high
11
12
13 vacuum (residual gas pressure 5×10^{-9} torr) with a Kratos AXIS Ultra DLD and a magnetic
14
15
16 immersion lens that consisted of a spherical mirror and concentric hemispherical
17
18
19 analyzers with a delay-line detector (DLD). An Al K α (1.486 KeV) monochromatic source
20
21
22 and He 1 (21.2 eV) source were used as excitation sources for the XPS and UPS
23
24
25 measurements, respectively. Ejected electrons were collected at a 90° angle from the
26
27
28 horizontal. The time-resolved PL measurements were taken on an inverted microscope
29
30
31 (Zeiss Axio Observer) equipped with an avalanche photodiode (Picoquant PDM series
32
33
34 with PicoHarp 300 timing electronics). For the PL lifetime measurements, a 400 nm
35
36
37 picosecond laser diode (70 ps pulse duration, 40 MHz repetition rate; PicoQuant)
38
39
40 excitation source was used, and a 400 nm band pass filter was placed after laser source
41
42
43 to purify the laser beam. A 100× objective lens with a numerical aperture of 0.9 (Zeiss,
44
45
46 Inc.) was used to focus the pulsed laser to a small spot of 1.6×10^{-6} cm² with an estimated
47
48
49 peak power density of 7.5 kW cm⁻².
50
51
52
53
54
55
56
57
58
59
60

STM/STS sample preparation and measurements

For the STM/STS studies, we transferred many flakes of WS_2 (with lateral dimensions of all grains greater than $10\ \mu\text{m}$) onto a commercial substrate with an atomic flat layer of Au (111) (200 nm thick) on mica so that the surface of the Au (111) / mica substrate was almost fully covered by monolayer WS_2 single crystals. The WS_2 / Au (111) / mica sample was annealed and sealed in vacuum, and then loaded onto our Omicron VT STM system. The base pressure of the system was 2×10^{-11} torr. Atomically resolved topographic and spectroscopic measurements were carried out on monolayer WS_2 samples at room temperature using a Pt/Ir STM tip.

ACKNOWLEDGEMENTS

The authors gratefully acknowledge joint support from the Army Research Office under the Multi-University Research Initiative (MURI) program, National Science Foundation under the Physics Frontier Center program for Institute for Quantum Information and Matter (IQIM), and Kavli Foundation. The authors thank Teddy Huang from the Bruker Nano Surface Company for helpful input regarding the CAFM data analysis, and Yen-Chun Chen for useful discussion on the CVD growth for TMDCs. The authors also acknowledge support from the Beckman Institute at the California Institute of Technology for access to facilities at the Molecular Materials Research Center.

ASSOCIATED CONTENT

Supporting Information

The Supporting Information is available free of charge on the ACS Publications website.

Supplementary Information Note 1 and Figures S1 and S2: CVD synthesis of monolayer WS₂ single crystals; Note 2 and Figure S3: Characteristic Raman mode

1
2
3 associated with defects/disorder in monolayer WS_2 single crystals; Note 3 and
4
5
6
7 Figure S4: XPS and UPS surface characterizations of WS_2 single crystals; Note 4
8
9
10 and Figure S5: Circularly polarized emission from as-grown monolayer h- WS_2
11
12
13 under σ_- 514.3nm excitation. Note 5 and Figure S6: Circularly polarized emission
14
15
16
17 from as-grown monolayer triangular shape WS_2 under σ_+ 514.3 nm excitation;
18
19
20
21 Note 6: Theoretical derivations for the circular polarization P_{circ} of neutral excitons
22
23
24 in the steady-state rate model; Note 7, Tables S1 and S2, and Figures S7:
25
26
27
28 Summary of the degree of polarization in MoS_2 and WS_2 at room temperature and
29
30
31 80 K.
32
33

34 AUTHOR CONTRIBUTIONS

35
36
37
38 W.-H. Lin and N.-C. Yeh conceived the research ideas. W.-H. Lin construct the CVD
39
40
41
42 system for h- WS_2 growth and participated in all the measurements and data analysis. W.-
43
44
45 S. Tseng contributed to the XPS measurement. C. M. Went and H. A. Atwater contributed
46
47
48 to the TRPL measurement. G. R. Rossman contributed to the Raman and PL mapping
49
50
51
52 measurements. W.-H. Lin and H. A. Atwater contributed to the STM/STS studies
53
54
55
56 presented in this manuscript using an Omicron VT STM system. M. L. Teague contributed
57
58
59
60

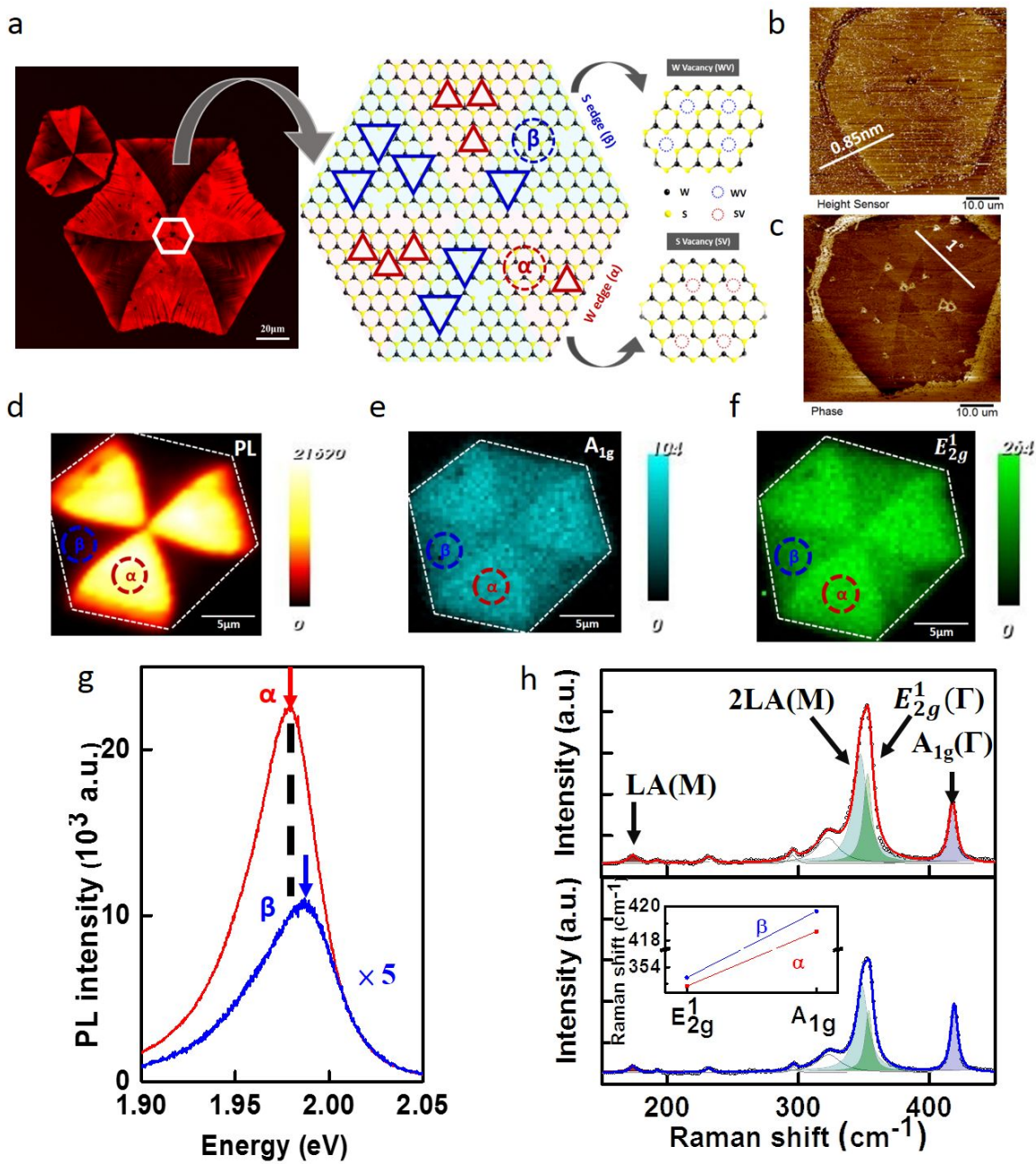
1
2
3 to the STM/STS studies with a homemade STM system in N.-C. Yeh's group to
4
5
6
7 independently verify the STM/STS results obtained by the Omicron VT STM system. W.-H.
8
9
10 Lin and N.-C. Yeh wrote the manuscript, and N.-C. Yeh supervised and coordinated the
11
12
13
14 project.
15
16
17
18
19
20

21 **COMPETING FINANCIAL INTERESTS**

22
23

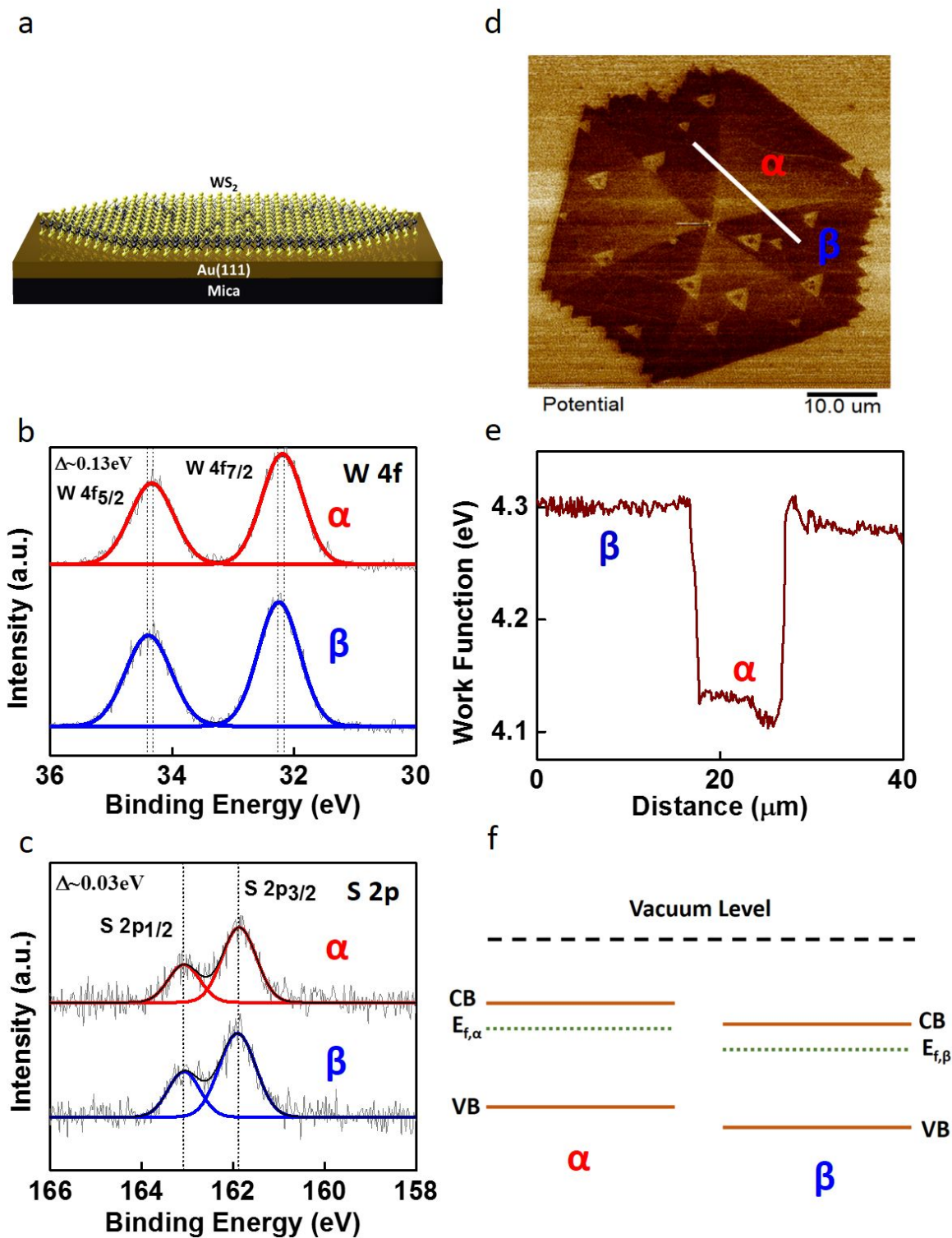
24 The authors declare no competing financial interests.
25
26
27
28
29
30
31
32
33
34
35
36
37
38
39
40
41
42
43
44
45
46
47
48
49
50
51
52
53
54
55
56
57
58
59
60

FIGURES



1
2
3
4
5
6
7
8
9
10
11
12
13
14
15
16
17
18
19
20
21
22
23
24
25
26
27
28
29
30
31
32
33
34
35
36
37
38
39
40
41
42
43
44
45
46
47
48
49
50
51
52
53
54
55
56
57
58
59
60

Figure 1. Monolayer h-WS₂ optical characterizations: **(a)** Left panel: Fluorescence images showing a radioactive hazard symbol-like optical emission pattern in the fluorescence intensity from a CVD-grown large monolayer WS₂ single crystal. Right panel: Schematic illustration of heterogeneous defect domains in single crystalline hexagonal WS₂. AFM measurements of **(b)** the surface topography and **(c)** the phase for a monolayer h-WS₂ single crystal. The scale bar is 10 μm. **(d)** PL intensity mapping of a monolayer h-WS₂ single crystal at the PL peak energy of 1.96 eV. The brighter PL domain (α) and darker PL domain (β) show threefold symmetry. Similar symmetries are also found in the Raman spectral intensity mapping for **(e)** the A_{1g} mode and **(f)** the E_{2g}¹ mode. Here the scale bars for (d-f) correspond to 5 μm. **(g)** Representative PL point spectra for the α - and β -domains of a monolayer h-WS₂. **(h)** Representative Raman spectra for the corresponding α - and β -domains as in (e) and (f).



1
2
3
4
5
6
7
8
9
10
11
12
13
14
15 **Figure 2.** Chemical bonding and work function characterization in heterogeneous domains: **(a)**
16 Schematic of the monolayer h-WS₂ on Au (111) / mica substrate. Selected XPS spectra of the α -
17 domain (top) and β -domain (bottom) for **(b)** W-4f and **(c)** S-2p, showing an upshift by ~ 0.13 eV
18 (~ 0.03 eV) in the W-4f (S-2p) peaks of the α -domain relative to those of the β -domain. The error
19 range for the binding energies determined by our XPS system is ± 0.025 eV. **(d)** KPFM image of
20 the heterogeneous domains of a monolayer h-WS₂. **(e)** Work function plot along the white line in
21 **(d)**. **(f)** Estimated Fermi levels ($E_{f,\alpha}$ and $E_{f,\beta}$) and the corresponding conduction band (CB) and
22 valence band (VB) positions of the α - and β -domains with respect to the vacuum level based on
23 KPFM.
24
25
26
27
28
29
30
31
32
33
34
35
36
37
38
39
40
41
42
43
44
45
46
47
48
49
50
51
52
53
54
55
56
57
58
59
60

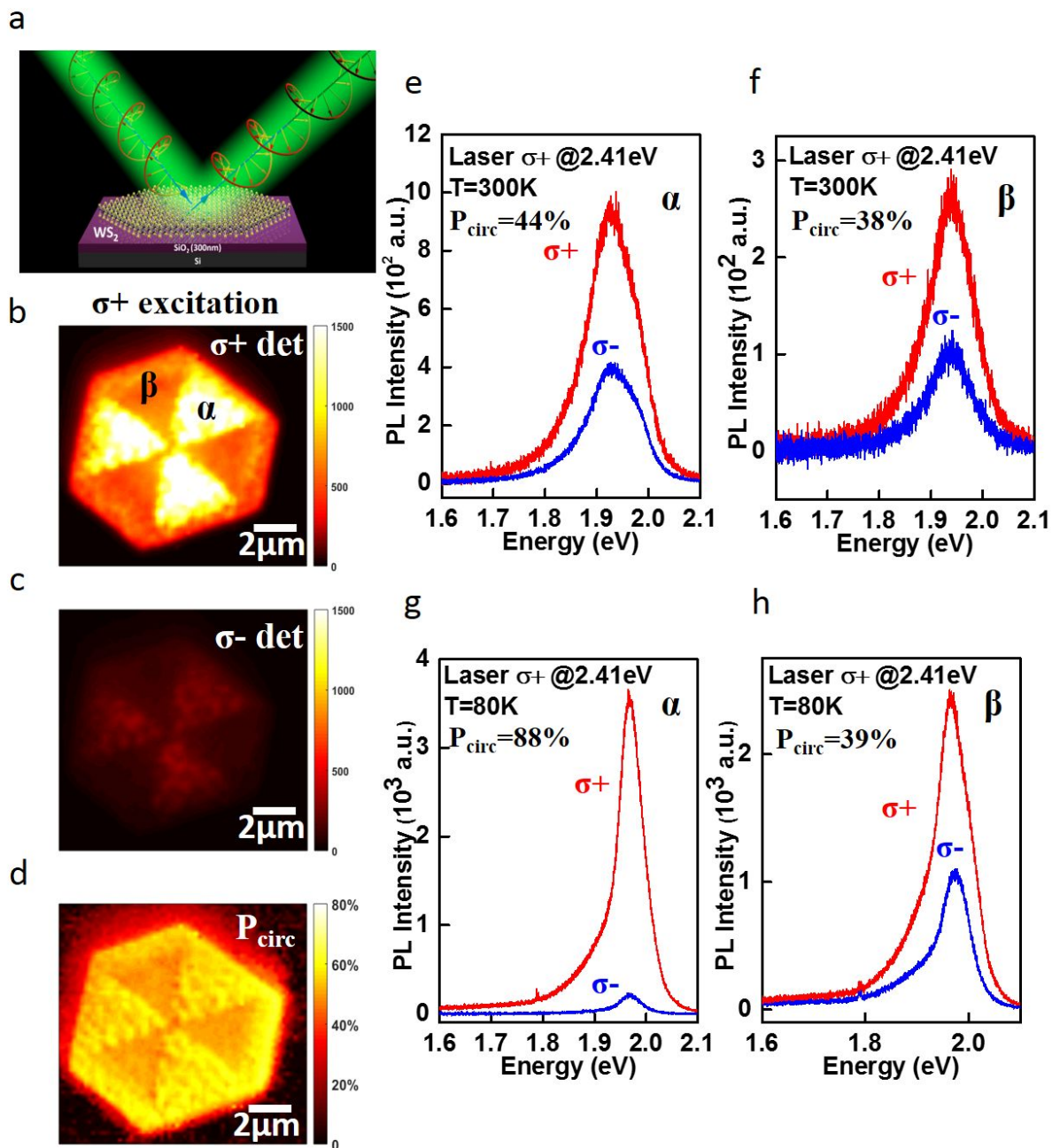
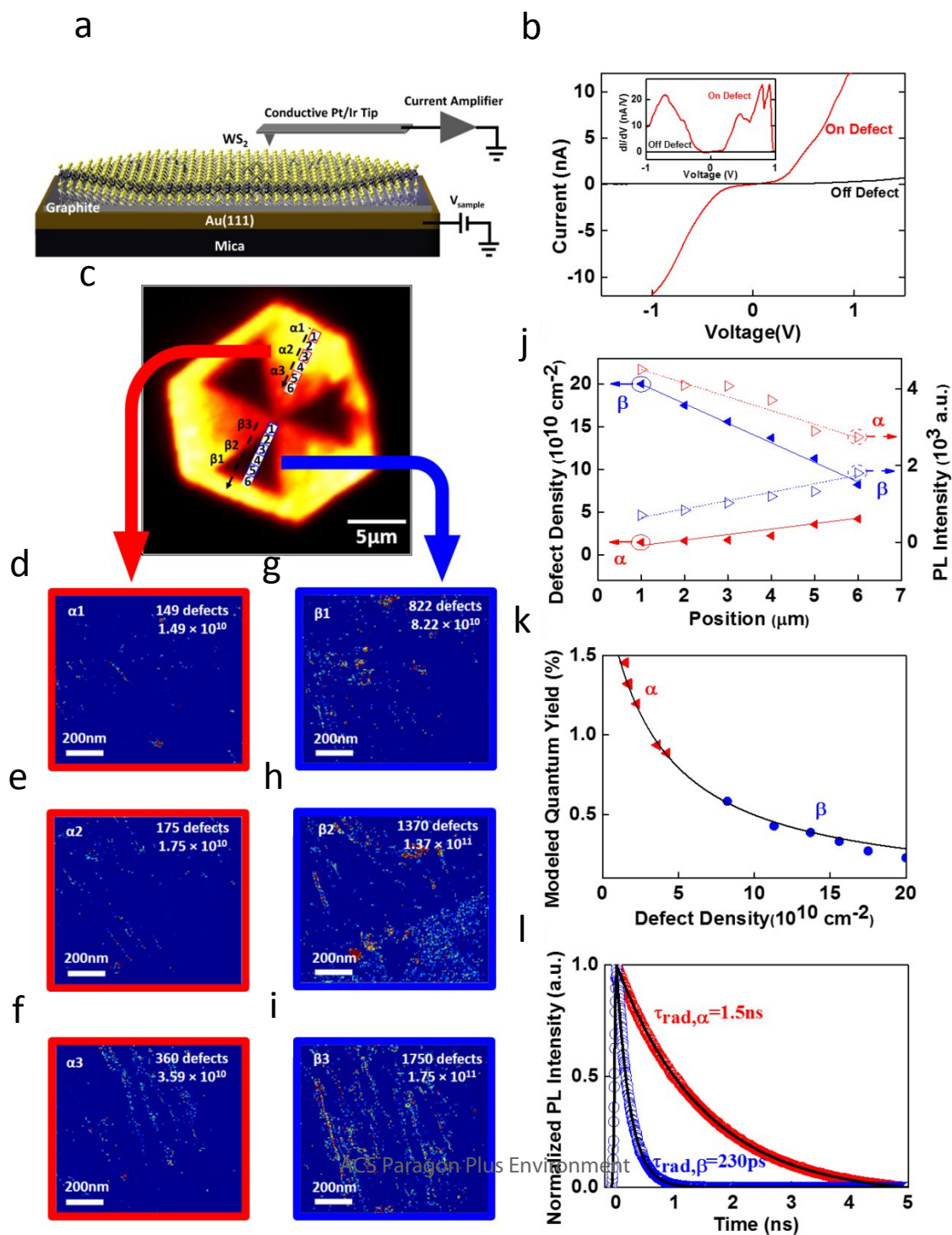


Figure 3. Circularly-polarized emission of monolayer h-WS₂ neutral excitons: **(a)** Schematic of circularly polarized emission on monolayer h-WS₂ under σ_+ 514nm (2.41 eV) excitation. **(b)** An intensity map for the σ_+ polarized emission and **(c)** an intensity map for the σ_- polarized emission. **(d)** A spatial map for the degree of valley polarization P_{circ} in a monolayer h-WS₂ single crystal. **(e-f)** Representative σ_+ (red) and σ_- (blue) PL intensity spectra taken at room temperature on the α - and β -domains, respectively. **(g-h)** Representative σ_+ (red) and σ_- (blue) PL intensity spectra taken at 80 K on the α - and β -domains, respectively.



1
2
3
4
5
6
7
8
9
10
11
12
13
14
15
16
17
18
19
20
21
22
23
24
25 **Figure 4.** Electrical characterizations of the monolayer h-WS₂: **(a)** Schematic illustration of the
26 experimental setup for the CAFM measurements. A CVD-grown thick multilayer graphene sample
27 was transferred onto an atomically flat Au (111) / mica substrate to provide a conductive backplane
28 for the measurement. A monolayer h-WS₂ sample was subsequently transferred onto the thick
29 multilayer graphene using the transfer method described in Methods. **(b)** I-V curves taken on a
30 defect and off a defect, showing a drastic difference in the conduction characteristics between a
31 defect region and the pristine h-WS₂. The inset figure in (b) shows the dI/dV characteristics
32 corresponding to the I-V curve in the main panel of (b). **(c)** PL map of the h-WS₂ sample, with
33 numbers 1 through 6 labeled in both one of the α -domains and one of the β -domains. The numbers
34 correspond to the locations where detailed CAFM maps were taken. **(d-i)** CAFM measurements
35 of the locations (α_1 , α_2 , α_3 , β_1 , β_2 , β_3) labeled in (c), exhibiting defect densities in the α -domain:
36 **(d)** $1.49 \times 10^{10} \text{ cm}^{-2}$ for α_1 , **(e)** $1.75 \times 10^{10} \text{ cm}^{-2}$ for α_2 , **(f)** $3.59 \times 10^{10} \text{ cm}^{-2}$ for α_3 , and in the β -domain:
37 **(g)** $8.22 \times 10^{10} \text{ cm}^{-2}$ for β_1 , **(h)** $1.37 \times 10^{11} \text{ cm}^{-2}$ for β_2 , **(i)** $1.75 \times 10^{11} \text{ cm}^{-2}$ for β_3 . **(j)** Defect density
38 and PL intensity as a function of position along the dashed line shown in (c) across the α - and β -
39 domains, showing apparent anti-correlation between the defect density and the PL intensity. **(k)**
40 The model presented in Eq. (7). The red points correspond to the PL measurements of the α -
41 domain, and blue points correspond to the PL measurements of the β -domain. **(l)** TRPL results,
42 showing PL decay profiles of the α - and β -domains. The black lines are fitting curves using a
43 single exponential decay function.
44
45
46
47
48
49
50
51
52
53
54
55
56
57
58
59
60

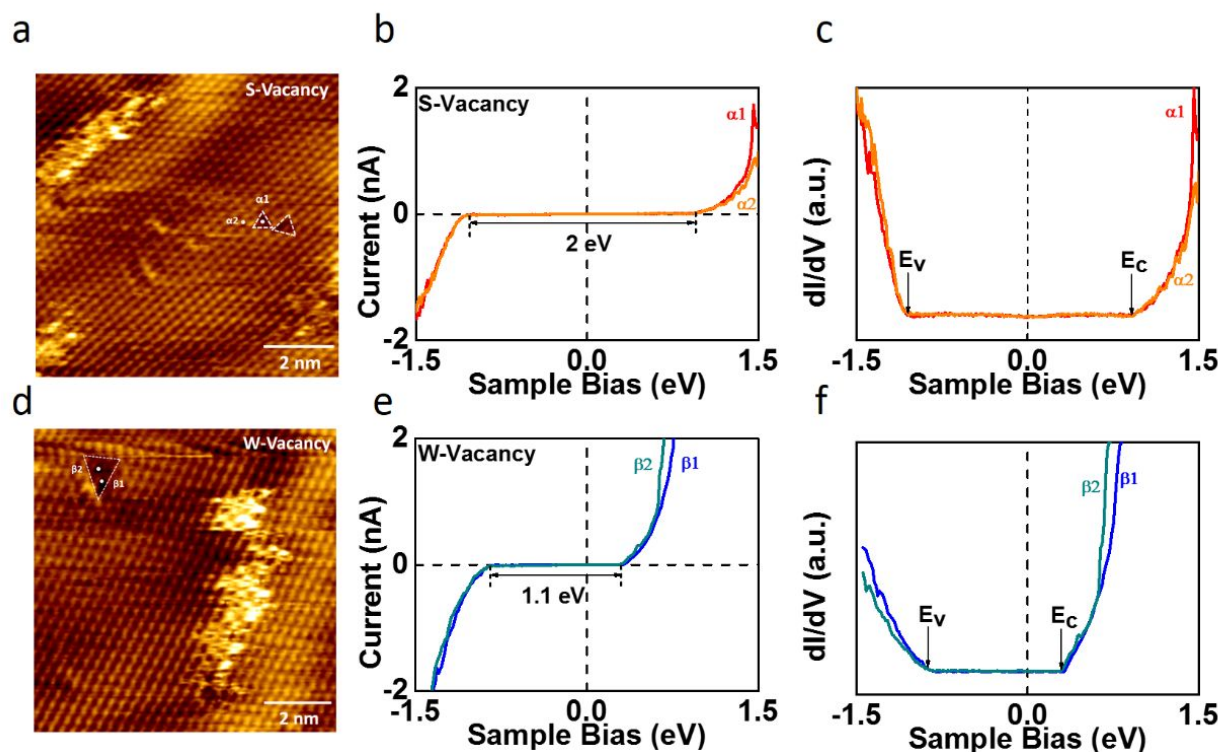
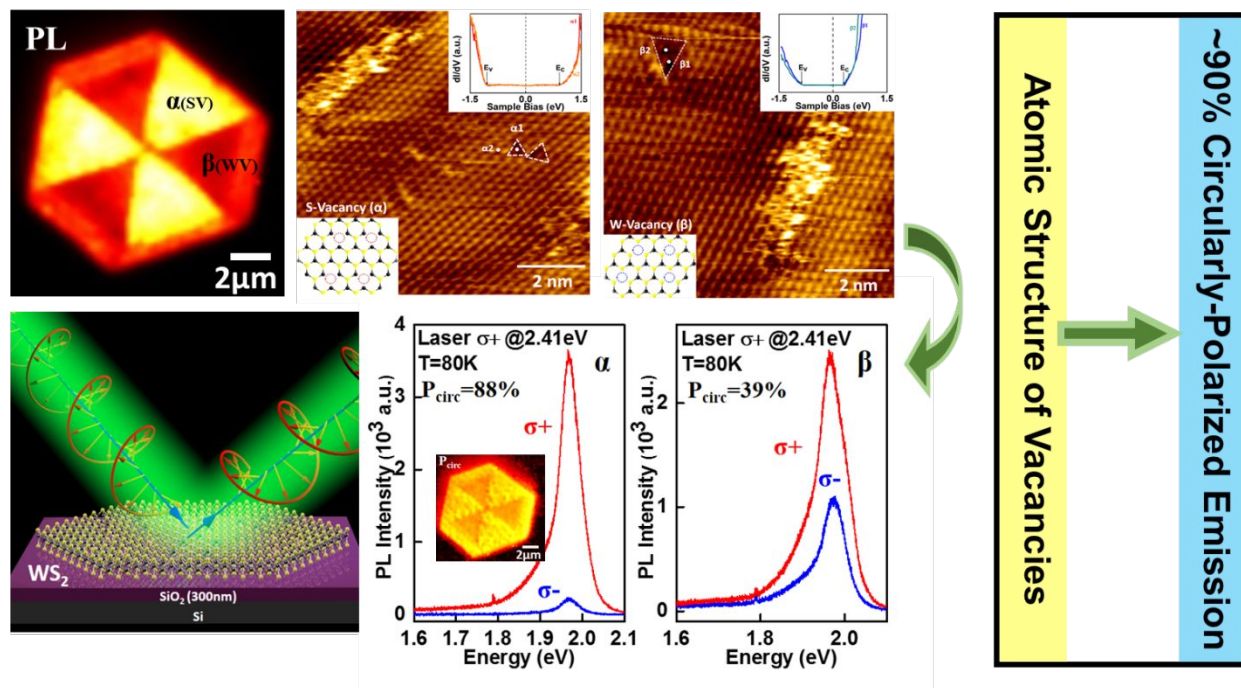


Figure 5. Scanning tunneling microscopic and spectroscopic studies of WS₂ monolayer: (a) Atomically-resolved of SVs (as indicated by the white triangles) on a sample of monolayer WS₂ on Au substrate. The topography was recorded under 0.7V, 1.2nA. Here the white solid circle $\alpha 1$ refers to the location of a SV in the center of a white triangle, and the white solid circle $\alpha 2$ refers to the location of a vacancy-free region. (b) Tunneling current (I) vs. sample biased voltage (V) spectra taken at a SV ($\alpha 1$) and defect free region ($\alpha 2$), showing consistent energy gaps of ~ 2.0 eV. Here the vertical dashed line corresponds to $E = 0$ (the Fermi level). (c) (dI/dV)-vs.- V spectra obtained from the regions $\alpha 1$ and $\alpha 2$ shown in (a). (d) Atomically-resolved WVs (shown by the white triangle) on a sample of monolayer WS₂ on Au substrate, with the topography recorded under 0.7V, 1.2nA. (e) I -vs.- V spectra taken at two WVs (white solid circles $\beta 1$ and $\beta 2$ in (d)), showing a reduced energy gap of 1.1 eV. The vertical dashed line corresponds to $E = 0$ (the Fermi level). (f) (dI/dV)-vs.- V spectra obtained from the regions $\beta 1$ and $\beta 2$ shown in (d). The tunneling spectra associated with the WVs are qualitatively similar to the CAFM measurements at non-radiative defect sites, suggesting that the WVs are responsible for the non-radiative defects that suppress PL and DOP in h-WS₂.

1
2
3
4
5
6
7
8
9
10
11
12
13
14
15
16
17
18
19
20
21
22
23
24
25
26
27
28
29
30
31
32
33
34
35
36
37
38
39
40
41
42
43
44
45
46
47
48
49
50
51
52
53
54
55
56
57
58
59
60

TOC Figure.



REFERENCES

1. Novoselov, K. S.; Jiang, D.; Schedin, F.; Booth, T. J.; Khotkevich, V. V.; Morozov, S. V.; Geim, A. K. Two-Dimensional Atomic Crystals. *P. Natl. Acad. Sci. USA* **2005**, *102*, 10451-10453.
2. Novoselov, K. S.; Mishchenko, A.; Carvalho, A.; Neto, A. H. C. 2D Materials and van der Waals Heterostructures. *Science* **2016**, *353*, 6298.
3. Mas-Balleste, R.; Gomez-Navarro, C.; Gomez-Herrero, J.; Zamora, F. 2D Materials: To Graphene and Beyond. *Nanoscale* **2011**, *3*, 20-30.
4. Wang, F.; Wang, Z. X.; Yin, L.; Cheng, R. Q.; Wang, J. J.; Wen, Y.; Shifa, T. A.; Wang, F. M.; Zhang, Y.; Zhan, X. Y.; He, J. 2D Library Beyond Graphene and Transition Metal Dichalcogenides: A Focus on Photodetection. *Chem. Soc. Rev.* **2018**, *47*, 6296-6341.
5. Geim, A. K. & Novoselov, K. S. The Rise of Graphene. *Nat. Mater.* **2007**, *6*, 183-191.
6. Novoselov, K. S. Nobel Lecture: Graphene: Materials in the Flatland. *Rev. Mod. Phys.* **2011**, *83*, 837-849.
7. Sheng, Y. W.; Rong, Y. M.; He, Z. Y.; Fan, Y.; Warner, J. H. Uniformity of Large-Area Bilayer Graphene Grown by Chemical Vapor Deposition. *Nanotechnology* **2015**, *26*, 395601.
8. Boyd, D. A.; Lin, W.-H.; Hsu, C.-C.; Teague, M. L.; Chen, C. C.; Lo, Y. Y.; Chan, W. Y.; Su, W. B.; Cheng, T. C.; Chang, C. S.; Wu, C.-I.; Yeh, N.-C. Single-Step Deposition of High-Mobility Graphene at Reduced Temperatures. *Nat. Commun.* **2015**, *6*, 6620.
9. Lin, W.-H.; Chen, T. H.; Chang, J. K.; Taur, J. I.; Lo, Y. Y.; Lee, W. L.; Chang, C. S.; Su, W. B.; Wu, C.-I. A Direct and Polymer-Free Method for Transferring Graphene

- 1
2
3 Grown by Chemical Vapor Deposition to Any Substrate. *ACS Nano* **2014**, *8*, 1784-
4 1791.
5
6
7
8
9 10. Gao, T.; Song, X. J.; Du, H. W.; Nie, Y. F.; Chen, Y. B.; Ji, Q. Q.; Sun, J. Y.; Yang, Y.
10 L.; Zhang, Y. F.; Liu, Z. F. Temperature-Triggered Chemical Switching Growth of In-
11 Plane and Vertically Stacked Graphene-Boron Nitride Heterostructures. *Nat. Commun.*
12 **2015**, *6*, 6835.
13
14
15
16
17 11. Dean, C. R.; Young, A. F.; Meric, I.; Lee, C.; Wang, L.; Sorgenfrei, S.; Watanabe, K.;
18 Taniguchi, T.; Kim, P.; Shepard, K. L.; Hone, J. Boron Nitride Substrates for High-
19 Quality Graphene Electronics. *Nat. Nanotechnol.* **2010**, *5*, 722-726.
20
21
22
23
24 12. Ci, L.; Song, L.; Jin, C. H.; Jariwala, D.; Wu, D. X.; Li, Y. J.; Srivastava, A.; Wang, Z.
25 F.; Storr, K.; Balicas, L.; Liu, F.; Ajayan, P. M. Atomic Layers of Hybridized Boron
26 Nitride and Graphene Domains. *Nat. Mater.* **2010**, *9*, 430-435.
27
28
29
30
31 13. Kim, K. K.; Hsu, A.; Jia, X. T.; Kim, S. M.; Shi, Y. S.; Hofmann, M.; Nezich, D.;
32 Rodriguez-Nieva, J. F.; Dresselhaus, M. S.; Palacios, T.; Kong, J. Synthesis of
33 Monolayer Hexagonal Boron Nitride on Cu Foil Using Chemical Vapor Deposition.
34 *Nano Lett.* **2012**, *12*, 161-166.
35
36
37
38
39
40 14. Lin, W.-H.; Brar, V. W.; Jariwala, D.; Sherrott, M. C.; Tseng, W.-S.; Wu, C.-I.; Yeh, N.-
41 C.; Atwater, H. A. Atomic-Scale Structural and Chemical Characterization of
42 Hexagonal Boron Nitride Layers Synthesized at the Wafer-Scale with Monolayer
43 Thickness Control. *Chem. Mater.* **2017**, *29*, 4700-4707.
44
45
46
47
48 15. Fang, H.; Chuang, S.; Chang, T. C.; Takei, K.; Takahashi, T.; Javey, A. High-
49 Performance Single Layered WSe₂ *p*-FETs with Chemically Doped Contacts. *Nano*
50 *Lett.* **2012**, *12*, 3788-3792.
51
52
53
54
55
56
57
58
59
60

- 1
2
3
4 16. Wang, H.; Yu, L. L.; Lee, Y. H.; Shi, Y. M.; Hsu, A.; Chin, M. L.; Li, L. J.; Dubey, M.;
5 Kong, J. & Palacios, T. Integrated Circuits Based on Bilayer MoS₂ Transistors. *Nano*
6 *Lett.* **2012**, 12, 4674-4680.
7
8
9
10 17. Zeng, H. L.; Dai, J. F.; Yao, W.; Xiao, D. & Cui, X. D. Valley Polarization in MoS₂
11 Monolayers by Optical Pumping. *Nat. Nanotechnol.* **2012**, 7, 490-493.
12
13
14 18. Jones, A. M.; Yu, H. Y.; Ghimire, N. J.; Wu, S. F.; Aivazian, G.; Ross, J. S.; Zhao, B.;
15 Yan, J. Q.; Mandrus, D. G.; Xiao, D.; Yao, W.; Xu, X. D. Optical Generation of Excitonic
16 Valley Coherence in Monolayer WSe₂. *Nat. Nanotechnol.* **2013**, 8, 634-638.
17
18
19 19. He, Z. Y.; Sheng, Y. W.; Rong, Y. M.; Lee, G. D.; Li, J.; Warner, J. H. Layer-Dependent
20 Modulation of Tungsten Disulfide Photoluminescence by Lateral Electric Fields. *ACS*
21 *Nano* **2015**, 9, 2740-2748.
22
23
24 20. Kim, I. S.; Sangwan, V. K.; Jariwala, D.; Wood, J. D.; Park, S.; Chen, K. S.; Shi, F. Y.;
25 Ruiz-Zepeda, F.; Ponce, A.; Jose-Yacamán, M.; Dravid, V. P.; Marks, T. J.; Hersam,
26 M. C.; Lauhon, L. J. Influence of Stoichiometry on the Optical and Electrical Properties
27 of Chemical Vapor Deposition Derived MoS₂. *ACS Nano* **2014**, 8, 10551-10558.
28
29
30 21. Han, H. V.; Lu, A. Y.; Lu, L. S.; Huang, J. K.; Li, H. N.; Hsu, C. L.; Lin, Y. C.; Chiu, M.
31 H.; Suenaga, K.; Chu, C. W.; Kuo, H. C.; Chang, W. H.; Li, L. J.; Shi, Y. M.
32 Photoluminescence Enhancement and Structure Repairing of Monolayer MoSe₂ by
33 Hydrohalic Acid Treatment. *ACS Nano* **2016**, 10, 1454-1461.
34
35
36 22. Li, H.; Tsai, C.; Koh, A. L.; Cai, L. L.; Contryman, A. W.; Fragapane, A. H.; Zhao, J. H.;
37 Han, H. S.; Manoharan, H. C.; Abild-Pedersen, F.; Nørskov, J. K.; Zheng, X. L.
38 Activating and Optimizing MoS₂ Basal Planes for Hydrogen Evolution Through the
39 Formation of Strained Sulphur Vacancies. *Nat. Mater.* **2016**, 15, 48.
40
41
42
43
44
45
46
47
48
49
50
51
52
53
54
55
56
57
58
59
60

- 1
2
3
4 23. Jeong, H. Y.; Jin, Y.; Yun, S. J.; Zhao, J.; Baik, J.; Keum, D. H.; Lee, H. S.; Lee, Y. H.
5 Heterogeneous Defect Domains in Single-Crystalline Hexagonal WS₂. *Adv. Mater.*
6 **2017**, 29, 1605043.
7
8
9
10 24. Lin, Y. C.; Li, S. S.; Komsa, H. P.; Chang, L. J.; Krasheninnikov, A. V.; Eda, G. K.;
11 Suenaga, K. Revealing the Atomic Defects of WS₂ Governing Its Distinct Optical
12 Emissions. *Adv. Funct. Mater.* **2018**, 28, 1704210.
13
14
15
16
17 25. Ly, T. H.; Yun, S. J.; Thi, Q. H.; Zhao, J. Edge Delamination of Monolayer Transition
18 Metal Dichalcogenides. *ACS Nano* **2017**, 11, 7534-7541.
19
20
21
22 26. Sheng, Y. W.; Wang, X. C.; Fujisawa, K.; Ying, S. Q.; Elias, A. L.; Lin, Z.; Xu, W. S.;
23 Zhou, Y. Q.; Korsunsky, A. M.; Bhaskaran, H.; Terrones, M.; Warner, J. H.
24 Photoluminescence Segmentation within Individual Hexagonal Monolayer Tungsten
25 Disulfide Domains Grown by Chemical Vapor Deposition. *ACS Appl. Mater. Inter.*
26 **2017**, 9, 15005-15014.
27
28
29
30
31
32
33 27. Kumar, P.; Verma, N. C.; Goyal, N.; Biswas, J.; Lodha, S.; Nandi, C. K.; Balakrishnan,
34 V. Phase Engineering of Seamless Heterophase Homojunctions with Co-Existing 3R
35 and 2H Phases in WS₂ Monolayers. *Nanoscale* **2018**, 10, 3320-3330.
36
37
38
39
40 28. Kormanyos, A.; Burkard, G.; Gmitra, M.; Fabian, J.; Zolyomi, V.; Drummond, N. D.;
41 Fal'ko, V. k·p Theory for Two-Dimensional Transition Metal Dichalcogenide
42 Semiconductors. *2D Mater.* **2015**, 2, 022001.
43
44
45
46
47 29. Ulstrup, S.; Katoch, J.; Koch, R. J.; Schwarz, D.; Singh, S.; McCreary, K. M.; Yoo, H.
48 K.; Xu, J. S.; Jonker, B. T.; Kawakami, R. K.; Bostwick, A.; Rotenberg, E.; Jozwiak, C.
49 Spatially Resolved Electronic Properties of Single-Layer WS₂ on Transition Metal
50 Oxides. *ACS Nano* **2016**, 10, 10058-10067.
51
52
53
54
55
56
57
58
59
60

- 1
2
3
4 30. Mak, K. F.; He, K.; Shan, J.; Heinz, T. F. Control of Valley Polarization in Monolayer
5 MoS₂ by Optical Helicity. *Nat. Nanotechnol.* **2012**, *7*, 494.
6
7
8 31. Kioseoglou, G.; Hanbicki, A. T.; Currie, M.; Friedman, A. L.; Gunlycke, D.; Jonker, B.
9 T. Valley Polarization and Intervalley Scattering in Monolayer MoS₂. *Appl. Phys. Lett.*
10 **2012**, *101*, 221907.
11
12
13
14
15 32. Cao, T.; Wang, G.; Han, W. P.; Ye, H. Q.; Zhu, C. R.; Shi, J. R.; Niu, Q.; Tan, P. H.;
16 Wang, E.; Liu, B. L.; Feng, J. Valley-Selective Circular Dichroism of Monolayer
17 Molybdenum Disulphide. *Nat. Commun.* **2012**, *3*, 887.
18
19
20
21
22 33. Yu, T.; Wu, M. W. Valley Depolarization due to Intervalley and Intravalley Electron-
23 Hole Exchange Interactions in Monolayer MoS₂. *Phys. Rev. B* **2014**, *89*, 205303.
24
25
26
27 34. Zhu, C. R.; Zhang, K.; Glazov, M.; Urbaszek, B.; Amand, T.; Ji, Z. W.; Liu, B. L.; Marie,
28 X. Exciton Valley Dynamics Probed by Kerr Rotation in WSe₂ Monolayers. *Phys. Rev.*
29 *B* **2014**, *90*, 161302.
30
31
32
33
34 35. Mai, C.; Semenov, Y. G.; Barrette, A.; Yu, Y. F.; Jin, Z. H.; Cao, L. Y.; Kim, K. W.;
35 Gundogdu, K. Exciton Valley Relaxation in a Single Layer of WS₂ Measured by
36 Ultrafast Spectroscopy. *Phys. Rev. B* **2014**, *90*, 041414.
37
38
39
40
41 36. Kioseoglou, G.; Hanbicki, A. T.; Currie, M.; Friedman, A. L.; Jonker, B. T. Optical
42 Polarization and Intervalley Scattering in Single Layers of MoS₂ and MoSe₂. *Sci. Rep.*
43 **2016**, *6*, 25041.
44
45
46
47 37. Wu, S. F.; Huang, C. M.; Aivazian, G.; Ross, J. S.; Cobden, D. H.; Xu, X. D. Vapor-
48 Solid Growth of High Optical Quality MoS₂ Monolayers with Near-Unity Valley
49 Polarization. *ACS Nano* **2013**, *7*, 2768-2772.
50
51
52
53
54
55
56
57
58
59
60

- 1
2
3
4 38. Sallen, G.; Bouet, L.; Marie, X.; Wang, G.; Zhu, C. R.; Han, W. P.; Lu, Y.; Tan, P. H.;
5 Amand, T.; Liu, B. L.; Urbaszek, B. Robust Optical Emission Polarization in MoS₂
6 Monolayers Through Selective Valley Excitation. *Phys. Rev. B* **2012**, *86*, 081301.
7
8
9
10 39. Lagarde, D.; Bouet, L.; Marie, X.; Zhu, C. R.; Liu, B. L.; Amand, T.; Tan, P. H.;
11 Urbaszek, B. Carrier and Polarization Dynamics in Monolayer MoS₂. *Phys. Rev. Lett.*
12 **2014**, *112*, 047401.
13
14
15
16
17 40. Hanbicki, A. T.; Kioseoglou, G.; Currie, M.; Hellberg, C. S.; McCreary, K. M.; Friedman,
18 A. L.; Jonker, B. T. Anomalous Temperature-Dependent Spin-Valley Polarization in
19 Monolayer WS₂. *Sci. Rep.* **2016**, *6*, 18885.
20
21
22
23
24 41. Zhu, B. R.; Zeng, H. L.; Dai, J. F.; Gong, Z. R.; Cui, X. D. Anomalously Robust Valley
25 Polarization and Valley Coherence in Bilayer WS₂. *P. Natl. Acad. Sci. USA* **2014**, *111*,
26 11606-11611.
27
28
29
30
31 42. Rosenberger, M. R.; Chuang, H. J.; McCreary, K. M.; Li, C. H.; Jonker, B. T. Electrical
32 Characterization of Discrete Defects and Impact of Defect Density on
33 Photoluminescence in Monolayer WS₂. *ACS Nano* **2018**, *12*, 1793-1800.
34
35
36
37
38 43. McCreary, A.; Berkdemir, A.; Wang, J. J.; Nguyen, M. A.; Elias, A. L.; Perea-Lopez,
39 N.; Fujisawa, K.; Kabius, B.; Carozo, V.; Cullen, D. A.; Mallouk, T. E.; Zhu, J.; Terrones,
40 M. Distinct Photoluminescence and Raman Spectroscopy Signatures for Identifying
41 Highly Crystalline WS₂ Monolayers Produced by Different Growth Methods. *J. Mater.*
42 *Res.* **2016**, *31*, 931-944.
43
44
45
46
47
48 44. Yu, Y. F.; Yu, Y. L.; Xu, C.; Cai, Y. Q.; Su, L. Q.; Zhang, Y.; Zhang, Y. W.; Gundogdu,
49 K.; Cao, L. Y. Engineering Substrate Interactions for High Luminescence Efficiency of
50 Transition-Metal Dichalcogenide Monolayers. *Adv. Funct. Mater.* **2016**, *26*, 4733-4739.
51
52
53
54
55
56
57
58
59
60

- 1
2
3
4 45. Ceballos, F.; Bellus, M. Z.; Chiu, H. Y.; Zhao, H. Ultrafast Charge Separation and
5 Indirect Exciton Formation in a MoS₂-MoSe₂ van der Waals Heterostructure. *ACS*
6 *Nano* **2014**, *8*, 12717-12724.
7
8
9
10 46. Wang, H.; Zhang, C.; Rana, F. Ultrafast Dynamics of Defect-Assisted Electron-Hole
11 Recombination in Monolayer MoS₂. *Nano Lett.* **2015**, *15*, 339-345.
12
13
14
15 47. Bhanu, U.; Islam, M. R.; Tetard, L.; Khondaker, S. I. Photoluminescence Quenching in
16 Gold - MoS₂ Hybrid Nanoflakes". *Sci. Rep.* **2014**, *4*, 5575.
17
18
19
20 48. Tongay, S.; Suh, J.; Ataca, C.; Fan, W.; Luce, A.; Kang, J. S.; Liu, J.; Ko, C.;
21 Raghunathanan, R.; Zhou, J.; Ogletree, F.; Li, J. B.; Grossman, J. C.; Wu, J. Q. Defects
22 Activated Photoluminescence in Two-Dimensional Semiconductors: Interplay between
23 Bound, Charged, and Free Excitons". *Sci. Rep.* **2013**, *3*, 2657.
24
25
26
27
28
29 49. Yuan, L. & Huang, L. B. Exciton Dynamics and Annihilation in WS₂ 2D
30 Semiconductors. *Nanoscale* **2015**, *7*, 7402-7408.
31
32
33
34 50. Ceballos, F. & Zhao, H. Ultrafast Laser Spectroscopy of Two-Dimensional Materials
35 Beyond Graphene. *Adv. Funct. Mater.* **2017**, *27*, 2657.
36
37
38
39 51. McCreary, K. M.; Currie, M.; Hanbicki, A. T.; Chuang, H. J.; Jonker, B. T.
40 Understanding Variations in Circularly Polarized Photoluminescence in Monolayer
41 Transition Metal Dichalcogenides. *ACS Nano* **2017**, *11*, 7988-7994.
42
43
44
45 52. Miller, B.; Steinhoff, A.; Pano, B.; Klein, J.; Jahnke, F.; Holleitner, A.; Wurstbauer, U.
46 Long-Lived Direct and Indirect Interlayer Excitons in van der Waals Heterostructures.
47 *Nano Lett* **2017**, *17*, 5229-5237.
48
49
50
51
52 53. He, J. Q.; He, D. W.; Wang, Y. S.; Cui, Q. N.; Ceballos, F.; Zhao, H. Spatiotemporal
53 Dynamics of Excitons in Monolayer and Bulk WS₂. *Nanoscale* **2015**, *7*, 9526-9531.
54
55
56
57
58
59
60

- 1
2
3
4 54. Zhao, P.; Amani, M.; Lien, D. H.; Ahn, G. H.; Kiriya, D.; Mastandrea, J. P.; Ager, J. W.;
5
6 Yablonovitch, E.; Chrzan, D. C.; Javey, A. Measuring the Edge Recombination Velocity
7
8 of Monolayer Semiconductors. *Nano Lett.* **2017**, *17*, 5356-5360.
9
10
11 55. Hanbicki, A. T.; Currie, M.; Kioseoglou, G.; Friedman, A. L.; Jonker, B. T. Measurement
12
13 of High Exciton Binding Energy in the Monolayer Transition-Metal Dichalcogenides
14
15 WS_2 and WSe_2 . *Solid State Commun.* **2015**, *203*, 16-20.
16
17
18 56. Amin, B.; Kaloni, T. P. & Schwingenschlögl, U. Strain Engineering of WS_2 , WSe_2 , and
19
20 WTe_2 . *RSC Adv.* **2014**, *4*, 34561.
21
22
23
24
25
26
27
28
29
30
31
32
33
34
35
36
37
38
39
40
41
42
43
44
45
46
47
48
49
50
51
52
53
54
55
56
57
58
59
60